Gaussian process-based online health monitoring and fault analysis of lithium-ion battery systems from field data

Cell Reports
Physical Science

CellPress
OPEN ACCESS

Article

Gaussian process-based online health monitoring and fault analysis of lithium-ion battery systems from field data

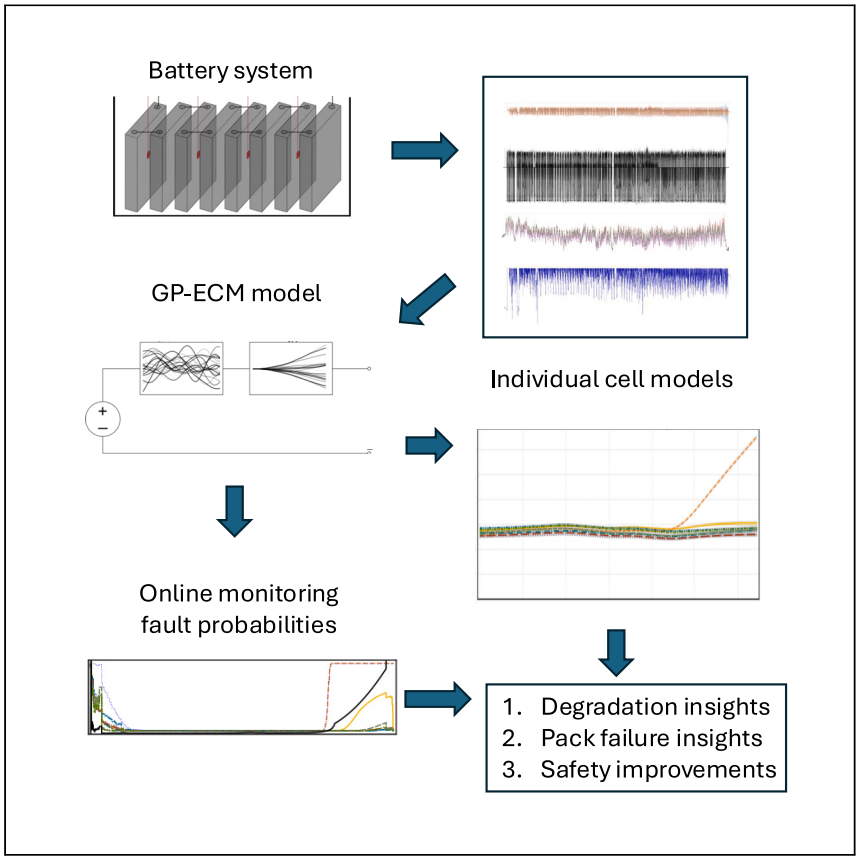

Improving battery safety is important to safeguard life and strengthen trust in lithium-ion batteries. Schaeffer et al. develop fault probabilities based on recursive spatiotemporal Gaussian processes, showing how batteries degrade and fail while publishing code and field data from 28 battery systems to benefit the community.

Joachim Schaeffer, Eric Lenz, Duncan Gulla, Martin Z. Bazant, Richard D. Braatz, Rolf Findeisen

rolf.findeisen@iat.tu-darmstadt.de

Highlights

Recursive spatiotemporal Gaussian processes are applied to lithium-ion battery field data

Online fault probabilities based on the resistance estimates are developed

The results provide insights into how battery systems degrade and fail in the field

We publish the BattGP Python library and the dataset comprising 28 battery systems

Schaeffer et al., Cell Reports Physical Science 5, 102258
November 20, 2024
Published by Elsevier Inc.
https://doi.org/10.1016/j.xcrp.2024.102258

Cell Reports
Physical Science

CellPress
OPEN ACCESS

Article

Gaussian process-based online health monitoring and fault analysis of lithium-ion battery systems from field data

Joachim Schaeffer,[1,2] Eric Lenz,[1] Duncan Gulla,[1] Martin Z. Bazant,[2,3] Richard D. Braatz,[2] and Rolf Findeisen[1,4,*]

SUMMARY

Health monitoring, fault analysis, and detection methods are important to operate battery systems safely. We apply Gaussian process resistance models on lithium-iron-phosphate (LFP) battery field data to separate the time-dependent and operating-point-dependent resistances. The dataset contains 28 battery systems returned to the manufacturer for warranty, each with eight cells in series, totaling 224 cells and 133 million data rows. We develop probabilistic fault detection rules using recursive spatiotemporal Gaussian processes. These processes scale linearly with the number of data points, allowing online monitoring. The fault analysis underlines that often, only a single cell shows abnormal behavior or a knee point, consistent with weakest-link failure for cells connected in series, amplified by local resistive heating. The results further the understanding of how battery packs degrade and fail in the field and demonstrate the potential of online monitoring. We open source the code and publish the dataset with this article.

INTRODUCTION

Lithium-ion batteries (LIBs) are essential for electric vehicles (EVs), grid storage, mobile applications, consumer electronics, and more. Over the last 30 years, remarkable advances have led to long-lasting cells with high energy efficiency and density.[1] The growth of production volume over the last decade is projected to continue[2,3] mainly due to EVs and stationary storage, both needed for the transition to a sustainable future. Safe operation of LIBs is vital to protect life and property and strengthen trust in LIBs. In the past, LIB fires erupted in many different applications, including EVs,[4] stationary storage,[5] and electric bicycles.[6] Monitoring batteries during operation is important to have a chance of detecting electrical or mechanical abuse of the system or the onset of accelerated cell degradation, which is critical to reducing the potential of such fires.

This article considers the design of Gaussian process (GP)-based health monitoring from battery field data, which are time series data consisting of noisy temperature, current, and voltage measurements corresponding to the system, module, and cell levels.[7] In real-world applications, the operational conditions are usually uncontrolled, i.e., the device is in the hands of the customer, who can use and potentially abuse the battery system. From a high level, the key task for the battery management system (BMS) is to ensure the safe operation of the battery system,[8] either onboard or potentially also leveraging the cloud[9] if further investigations or compute power are needed. Field data are critical for improving BMSs,

[1]Control and Cyber-Physical Systems Laboratory Technical, University of Darmstadt, 64289 Darmstadt, Germany

[2]Department of Chemical Engineering, Massachusetts Institute of Technology, Cambridge, MA 02139, USA

[3]Department of Mathematics, Massachusetts Institute of Technology, Cambridge, MA 02139, USA

[4]Lead contact

*Correspondence: rolf.findeisen@iat.tu-darmstadt.de

https://doi.org/10.1016/j.xcrp.2024.102258

understanding how batteries age in the field, and detecting faults early under realistic battery operating conditions.[7,10] Furthermore, openly available health monitoring algorithms and software are important for regulation. One example is the battery passport.[2] A critical bottleneck in pushing the field of battery monitoring forward has been the lack of published battery field data.[11] Open sourcing of the code and data is a key contribution of this article.

Many methods are available for modeling the cycling and degradation behavior of battery cells and systems.[12–14] Roughly, these battery models can be categorized as empirical models,[15,16] machine learning models,[17–22] first-principles models (also known as [aka] physics-based aka mechanistic),[23–25] and hybrid models, which combine first-principles and machine learning models.[26,27] Choosing an appropriate model is essential to optimally using the available data.[12] Physics-based battery models such as pseudo-two-dimensional (P2D) and single-particle models (SPMs) are challenging to parameterize with field data where often no or only a few physical cell parameters are known in combination with sensor noise and bias as well as low time resolution. Equivalent circuit models (ECMs) are an alternative because they are easier to parameterize with limited data[13] and are applicable to field data.[28]

Faults are abnormal events that cause the system to behave in an unintended way or stop operating. Battery system faults can be auxiliary, sensor, or battery faults. Furthermore, faults can potentially cause safety threats to a system and its environment, emphasizing the importance of monitoring and early fault detection. Fault detection methods can be categorized as signal based or model based. Much research considers fast signal-based fault detection for battery systems.[29–31] A few examples of commonly used methods include normalized voltage-based methods,[32] analysis of correlation coefficients of cell voltages,[33,34] and sample entropy-based methods.[35]

Model-based fault detection methods are complementary to signal-based fault detection. While model-based fault detection methods are usually computationally more complex and slower, they can potentially detect certain faults earlier and improve robustness.[36–42] In particular, battery system faults, which are often due to slow processes, such as battery degradation, can be addressed by a model to estimate the state of health (SOH) of batteries.[28,43,44] It is commonly observed that slow capacity decay is followed by accelerated degradation, yielding a knee-shaped capacity decay curve as a function of charge throughput.[45] Consequently, the cell will behave very differently from the remaining cells.

In this work, we analyze and model the resistance of each cell in LIB systems based on field data. We build on a hybrid approach of using GPs and ECMs developed by Aitio et al. for single-cell lead-acid batteries[28] and adapt the model to lithium-iron-phosphate (LFP) battery systems. This hybrid approach approximates two decoupled series resistances, i.e., an operational point-dependent resistance and a temperature-dependent resistance.[28] First, we show exact GP results using 40,000 data points for each cell. Next, we show recursive spatiotemporal GP[28,46–48] results based on all selected data points, resulting in millions of analyzed data points in total. We then develop fault probabilities, allowing us to monitor the homogeneity of cell resistances and the probability of a single cell exceeding a maximum resistance threshold, which are important for detecting the onset of different types of battery system faults. The derivations are motivated by field data from 28 portable LIB systems consisting of eight cells in series, totaling 224 cells that were in use for up

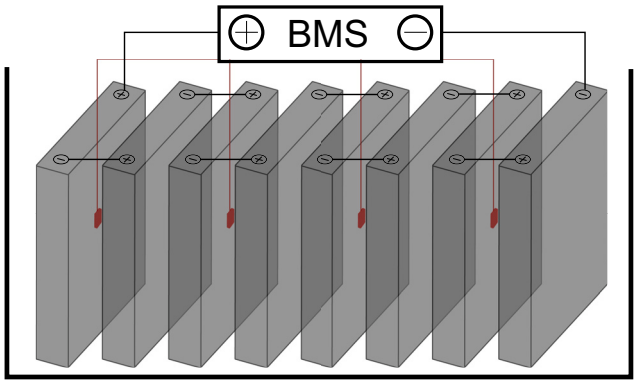

Figure 1. Battery system
Sketch of 8 prismatic cells in gray, with temperature sensors in red. The temperature sensors are shared by two cells.

to 5 years. All analyzed systems were returned to the manufacturer for warranty claims, where the data were recovered. Analyzing the dataset and modeling results furthers the understanding of how these battery packs fail. This article makes the field data and associated Python package BattGP available as open source. This dataset can be used to develop and test approaches for SOH estimation, fault detection, and health monitoring. We hope the battery modeling community will use this dataset for further development. To the authors' knowledge, this is one of the first large publicly available LIB field dataset containing data from many independent systems and multiple years of operation that allows us to study faults. Recently, another large battery field data set was published by Figgener et al.[49] The study by Figgener et al. focuses on capacity fade, whereas this article's data set is from battery systems that degraded and had faulty behavior. The two data sets thus complement each other.

RESULTS AND DISCUSSION

Battery system and field dataset

The dataset contains data from 28 portable 24 V LFP battery systems with approximately 160 Ah nominal capacity. Each system's specific use case is unknown, but battery systems of this size are typically used as power sources for recreational vehicles, solar energy storage, and more.

All battery systems in this dataset showed some form of unsatisfactory behavior and were returned to the manufacturer. Many reasons can cause a consumer to return a battery to the manufacturer for maintenance. The user's individual decisions may be motivated by personal judgment, BMS warnings, or customer support advice. This dataset comprises a very small fraction of batteries sold of this version. Therefore, this dataset is biased and not representative of the operational data of the entire population of this system version. This article's battery system type was replaced with an improved version. The battery system manufacturer provided the dataset for this study and allowed its open-source release under the condition of anonymity.

Some time series contain data gaps, either because the system was fully switched off, the user tampered with it and its data storage unit, or for other unknown reasons. Furthermore, the exact manufacturing and shipping dates are unavailable, making it impossible to precisely reconstruct charge throughput and rest period durations for all systems.

Table 1. System and data specifications	
Technical specification	
Nominal voltage	24 V
Nominal capacity	≈160 Ah
No. of cells	8 (series)
No. of current sensors	1
No. of voltage sensors	9
No. of temperature sensors	4
No. of cell balancing current sensors	8
Dataset	
No. of systems	28
Total number of cells	224
Total rows of data	133 M
Median of measurement intervals	5 s

Each battery system consists of 8 prismatic cells in series. Each system has one load current sensor, and each cell has one voltage sensor. The four temperature sensors are placed between adjacent cells, i.e., each temperature sensor is shared by two cells (Figure 1). Furthermore, the battery systems have active cell balancing. The available measurements for the systems vary from a single month to 5 years. Consequently, the number of data rows per system varies from several thousand to millions, depending on the duration of battery operation. The dataset contains a total of 133 million rows of measurements (Table 1).

The estimated probability densities of usage conditions (Figure 2) demonstrate the widely varying operational conditions. For example, many temperature measurements are below room temperature, suggesting that some systems were operated outdoors or in unheated environments. The observed depth of discharges (DODs) are predominantly limited to the upper half of the state of charge (SOC) range, and much time was spent fully charged for most systems. The distribution of voltage shows that some batteries were overcharged (>3.6 V), undercharged (<2.0 V), or both at some point. Furthermore, battery systems 3, 4, and 16 have discharge current outliers >1,000 A, suggesting a shortcut or inrush current due to improper installation, abuse, or a sensor error. It is not possible to further disentangle the reasons for these abnormally high discharge currents and over-/undercharging. There is a lot of uncertainty associated with how the user installed the system and which equipment was connected because the systems are portable and suitable for many different applications.

Exemplary data visualization and analysis

We analyze 24.2 million rows of data associated with battery system 8, which was operated for approximately 5 years (Figure 3). The system was switched on in November 2016, but frequent usage only started about a year later. The end of continuous usage is around December 2021. However, the system kept logging data for a couple more months afterward. The temperature profile shows seasonal variations, with higher temperatures during the Northern hemisphere's summer months. Furthermore, voltage measurements and estimated SOC show that the system was primarily operated between 60% to 100% SOC, with occasional discharges below 40%. Around September 2020, the usage pattern changes, as can be seen by the current and SOC patterns. The mean subtracted cell voltages,

$$\tilde{u}_i(t) = u_i(t) - \frac{1}{n-1}\sum_{j,j\neq i}^{n} u_j(t), \qquad \text{(Equation 1)}$$

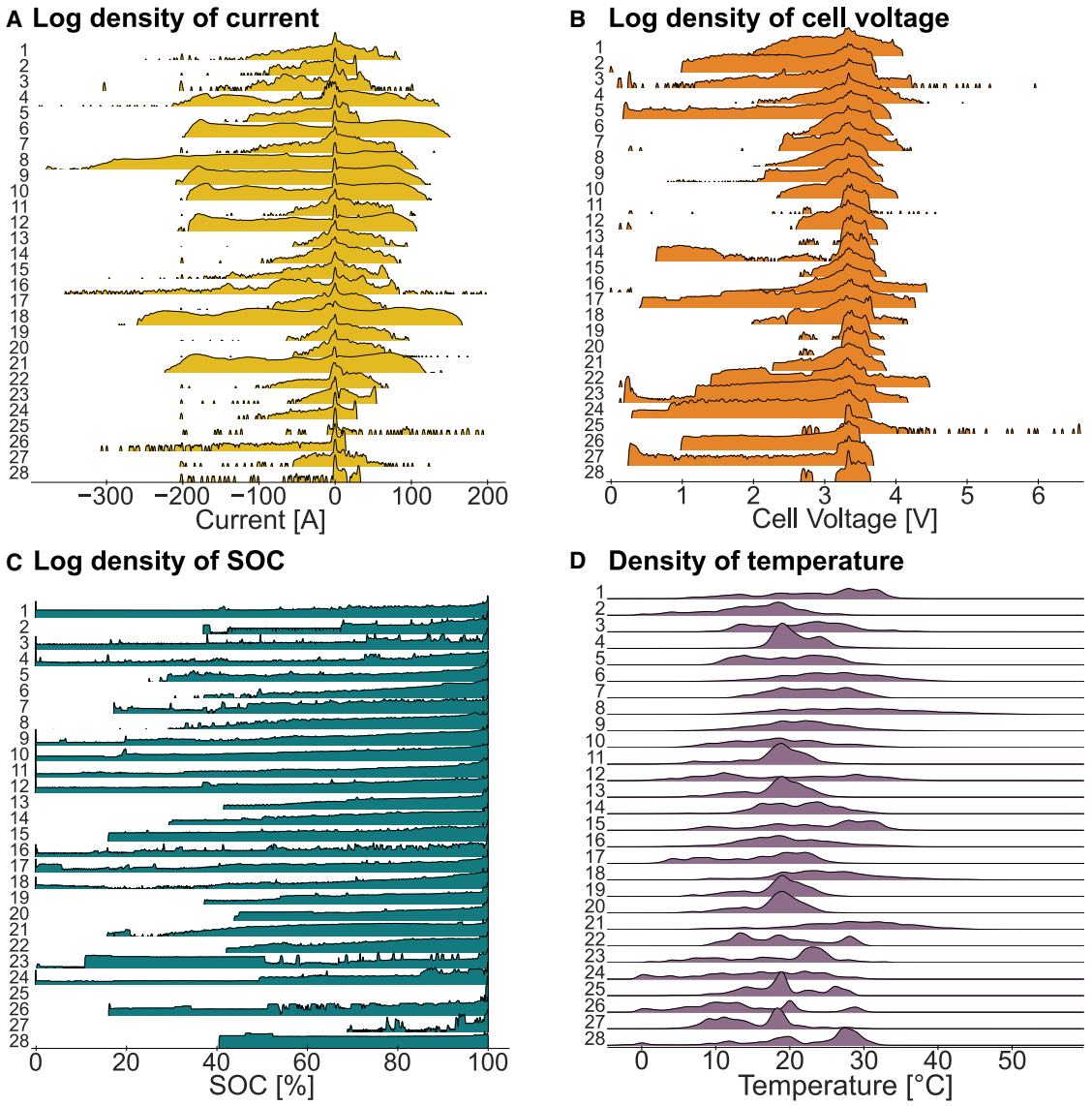

Figure 2. PDF estimates for each system

Log probability density function (log-PDF) of current (A), log-PDF of cell voltages (B), log-PDF of SOC (C), and PDF of temperatures (D).

where $u_i(t)$ is the voltage of cell i at time t and n is the number of cells, show average deviations below 0.1 V for the first 2 years of operation (Figure 3B). With increasing usage, i.e., increasing charge throughput and time and therefore also degradation, the average mean subtracted voltages increase, an indicator that individual cells age differently, likely due to cell-to-cell variations,[50,51] and as a consequence, the system is less balanced. Similarly, the voltage standard deviations,

$$\sigma_u(t) = \sqrt{\frac{1}{n-1}\sum_{i=1}^{n}(u_i(t) - \mu(t))^2}, \text{where } \mu(t) = \frac{1}{n}\sum_{i=1}^{n}u_i(t), \qquad \text{(Equation 2)}$$

are below 0.05 V for the first years; however, toward the end of use, the standard deviation of cell voltages increases significantly.

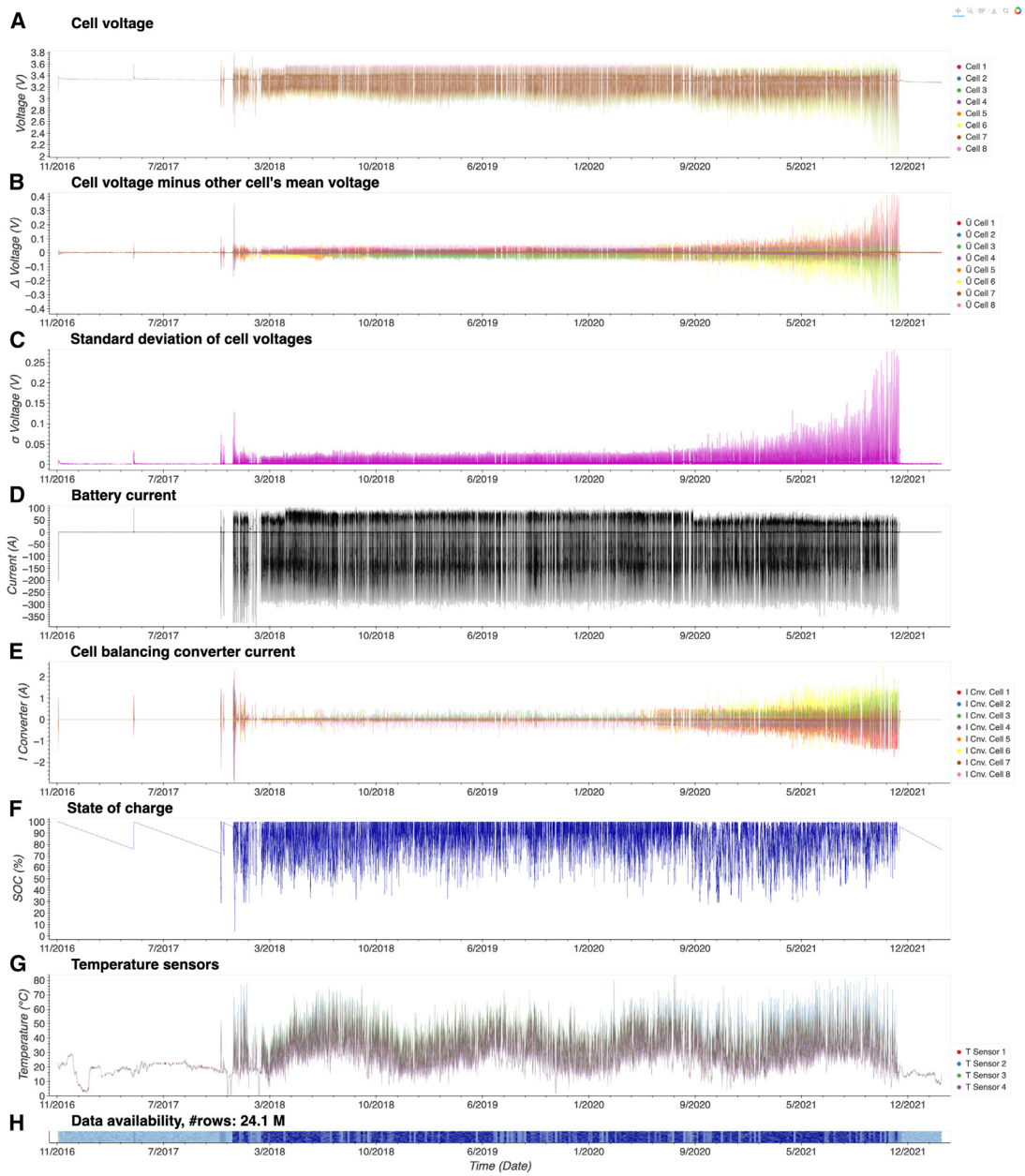

Figure 3. Data visualization of battery system 8

(A) Cell voltages.
(B) Cell voltages with mean of other cells subtracted.
(C) Cell voltage standard deviation.
(D) Battery system current.
(E) Cell balancing converter current.
(F) State of charge.
(G) Temperatures (each temperature sensor neighbors two cells; see Figure 1).
(H) Data availability.
Figures S10–S37 show the data visualization for all systems.

To summarize, the data analysis of system 8 shows heavy usage over a 5-year period, totaling about 1,531 equivalent full cycles. However, based on the data visualization, it is challenging to further understand how cells degraded, whether certain cells

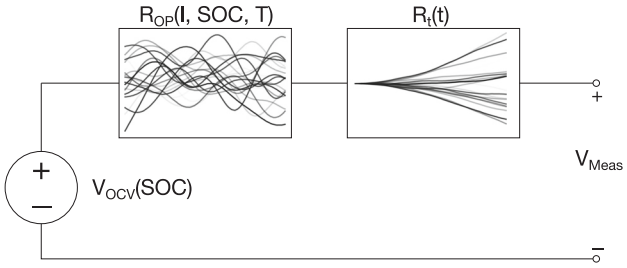

Figure 4. Visualization of the ECM and GP kernels

ECM with two series resistors and illustrations of random draws from the corresponding kernel functions. The radial basis function kernel depends on current, SOC, and temperature, and the Wiener velocity kernel depends on time, as suggested by Aitio et al.[28]

degraded more than others, or when the system might fail. Next, we explore how to use the battery data for internal state estimation suitable for tracking the aging behavior of the individual cells.

GP equivalent circuit battery systems modeling

GPs are suitable for modeling the time- and operating point behavior of batteries.[28] GPs, $f(x) \sim \mathrm{GP}(\mu(x), k(x,x'))$, are nonparametric probabilistic models defining a distribution of functions. GPs are defined by a mean function $\mu(x)$ and a covariance function $k(x, x')$, where $x, x' \in \mathcal{X}^D$ and $\mathcal{X}^D$ is the input space with dimension D. The modeled response y follows a Gaussian distribution, as does any marginal distribution.[52] GPs are a flexible modeling framework excelling in the case of limited data by making a point estimate and modeling the covariance associated with the prediction.

We base our analysis on a GP-ECM model that uses an ECM consisting of two series resistors modeled by two additive kernels (Figure 4).[28] For simplicity, we do not include resistor-capacitor (RC) circuit elements in the model; however, extending GP-ECM models to include RC circuit elements is an active research area.[48] Here, the first resistor is modeled by a radial basis function (RBF) kernel taking the current, SOC, and temperature as inputs and is, therefore, only dependent on the operating point of the battery. The resulting RBF function estimates are infinitely many times differentiable and thus smooth, in agreement with what is expected experimentally (see Anseán et al.[53] and Figure S1). A non-stationary Wiener velocity (WV) kernel models the second series resistor and depends only on time, based on the assumption that the time-dependent resistance will only increase due to degradation. See Duvenaud[54] for more information on kernels. The underlying assumption of this "R-R" model is that the operating-point-dependent equivalent circuit internal resistance and time-dependent resistance are additive. This assumption, while not exactly fulfilled by LIBs, is reasonable, allowing us to approximate and extract the equivalent circuit time-dependent resistance, i.e., a proxy of degradation.

In addition, the open-circuit voltage (OCV) curve is needed. However, no precise OCV curve was available for the battery cells under consideration. Therefore, we linearly approximate the OCV plateau region of LFP (Figure S2). Physically, the linear OCV model approximates the distribution of particle-size-dependent nucleation barriers[55] for a porous electrode with a particular distribution of LFP particle sizes.[56] In practice, any deviation from the true OCV will lead to a biased resistance; however, this bias is only a function of SOC and will, therefore, affect mainly the SOC dimension of the RBF kernel (Figure S1). Furthermore, even if a precisely measured OCV would be available at the beginning of life, the OCV is expected to change with degradation.

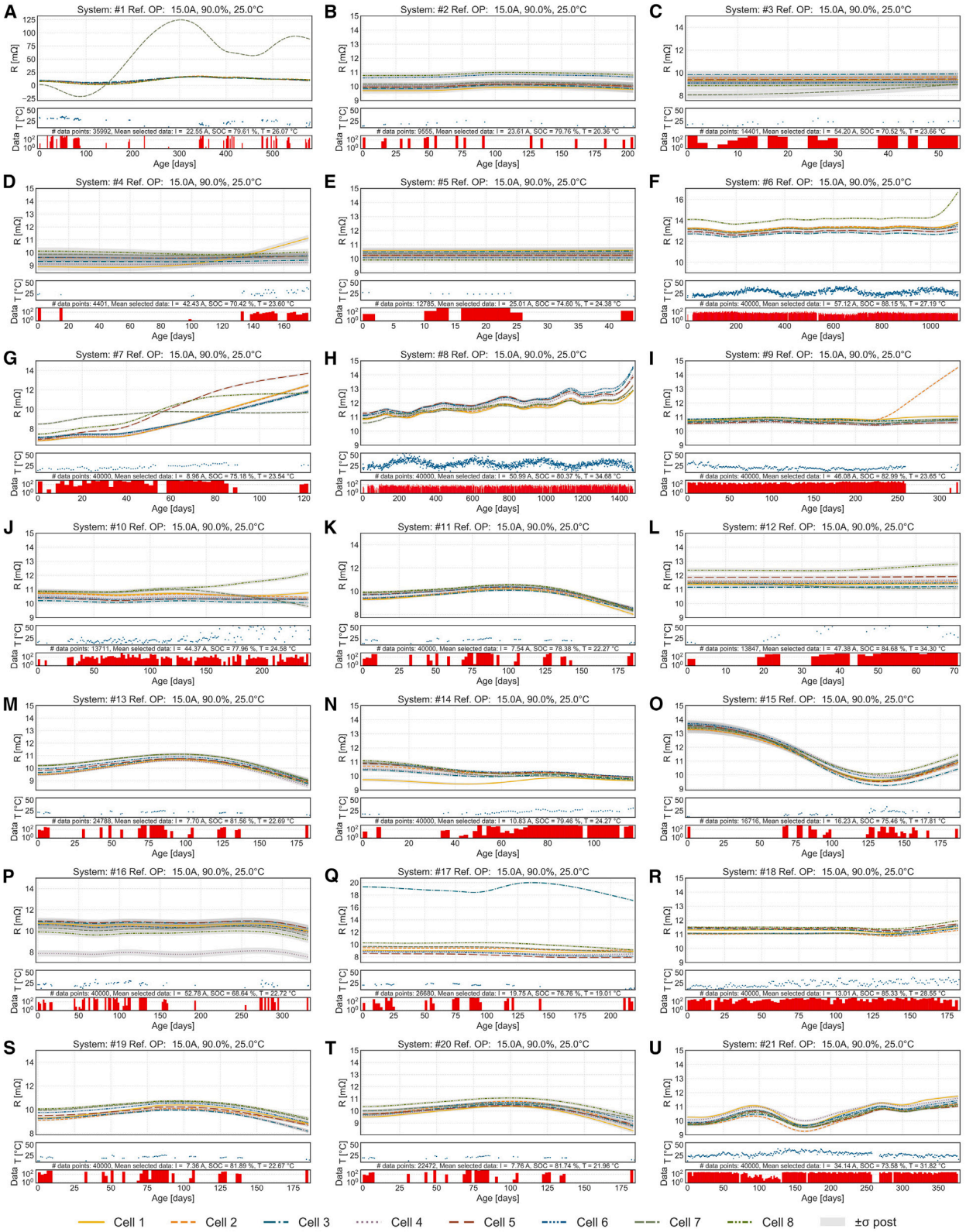
A System: #1 Ref. OP: 15.0A, 90.0%, 25.0°C
B System: #2 Ref. OP: 15.0A, 90.0%, 25.0°C
C System: #3 Ref. OP: 15.0A, 90.0%, 25.0°C
D System: #4 Ref. OP: 15.0A, 90.0%, 25.0°C
E System: #5 Ref. OP: 15.0A, 90.0%, 25.0°C
F System: #6 Ref. OP: 15.0A, 90.0%, 25.0°C
G System: #7 Ref. OP: 15.0A, 90.0%, 25.0°C
H System: #8 Ref. OP: 15.0A, 90.0%, 25.0°C
I System: #9 Ref. OP: 15.0A, 90.0%, 25.0°C
J System: #10 Ref. OP: 15.0A, 90.0%, 25.0°C
K System: #11 Ref. OP: 15.0A, 90.0%, 25.0°C
L System: #12 Ref. OP: 15.0A, 90.0%, 25.0°C
M System: #13 Ref. OP: 15.0A, 90.0%, 25.0°C
N System: #14 Ref. OP: 15.0A, 90.0%, 25.0°C
O System: #15 Ref. OP: 15.0A, 90.0%, 25.0°C
P System: #16 Ref. OP: 15.0A, 90.0%, 25.0°C
Q System: #17 Ref. OP: 15.0A, 90.0%, 25.0°C
R System: #18 Ref. OP: 15.0A, 90.0%, 25.0°C
S System: #19 Ref. OP: 15.0A, 90.0%, 25.0°C
T System: #20 Ref. OP: 15.0A, 90.0%, 25.0°C
U System: #21 Ref. OP: 15.0A, 90.0%, 25.0°C
R [mΩ]
Data T [°C]
Age [days]
Cell 1
Cell 2
Cell 3
Cell 4
Cell 5
Cell 6
Cell 7
Cell 8
±σ post

Figure 5. Time-dependent resistance estimates from Wiener velocity kernel

Evaluation of the time-dependent Wiener velocity kernel equivalent circuit resistance for up to 40,000 randomly selected data points after downselection. Only systems for which >2,000 data points after downselection are available are shown (21 systems). Each subplot shows the equivalent circuit resistance for each cell, with the reference operating point set to −15 A, 90% SOC, and 25° C (top); the average daily temperature of all sensors (middle); and a logarithmically scaled bar plot in red visualizing the available data (bottom). The results are described in more detail in Table 2.

An advantage of using a GP in comparison to other ways of filtering or smoothing the resistances is that the GP framework allows separating the time-dependent resistance from the operating-point-dependent resistance. The GP estimated resistances might not be identical to the internal cell resistance; see Islam et al.[57] for a discussion. However, here we are mainly concerned with monitoring changes in the time-dependent battery resistance.

The GP-ECM algorithm consists of the following steps for a single cell. First, voltage, current, SOC, and time are extracted and downselected. The aim is to select data points with significant information for the learning tasks and to avoid sparse extreme conditions where few data are available or the simple R-R model is less suitable. We use discharging sections only because, in the dataset, there are more dynamics during discharging. Further selection criteria outlined in the experimental procedures section are applied to limit the considered SOC window, discharge current range, and temperature conditions (Table 3). We selected the latest section with no gaps longer than 100 days and required at least 2000 valid data points, resulting in a selection of 21 systems for modeling.

Based on the pack layout, eight cells in series, and one parallel string (8s1p), we generate a model for each cell, resulting in eight models for each battery system. We use exact GPs to get an overview of the dataset but move to recursive spatio-temporal GPs in the next section for online monitoring (see the experimental procedures section for more details). To keep the space and computational complexity feasible for the exact GP, we further downselect each cell to a maximum of 40,000 measurements by selecting data with linearly spaced indices of the preselected data. The hyperparameters are optimized as outlined in the experimental procedures section. Identical hyperparameters are used for all battery systems because the hyperparameters characterize the system behavior, and all systems are identical in construction. Even though the batteries were operated in different applications with different average operating points, GPs can handle these differences. The GP inference takes, on average, 11 s per cell on an NVIDIA A100 GPU using 40,000 data points.

The GP modeling results (Figure 5) show the time-dependent resistance modeled by the WV kernel at the same reference operating point for all systems (−15 A, 90% SOC, 25°C). Table 2 gives an overview of the equivalent full cycle count, available data, section length modeled by the GP, and intriguing cells. In addition, Table 2 describes the modeling results for each system in more detail. Further modeling results that use the mean of each system's selected data as a reference operating point (Figure S9) support the conclusions in Table 2.

Systems 6, 8, and 21 show a high range of operating temperatures, likely due to seasonal temperature variations. These variations pose challenges for the GP framework because the WV kernel resistance estimates are affected by the temperature variations, with lower temperatures leading to higher resistance estimates.[53,58] Consequently, using the resistance time derivative for forecasting as suggested by Aitio et al.[28] for lead-acid batteries appears challenging for LIBs.

Table 2. Overview of GP modeling results

Subplot, system ID	Equivalent full cycles	Max age (days)	GP section (days)	Intriguing cells	Comments
a, 1	14	1,402	580	7	cell 7 behaves differently from the other cells
b, 2	6	982	204	6, 8	cells 6 and 8 show a slightly higher resistance than the other cells
c, 3	11	160	54	7	cell 7 shows an upward resistance trend, while other cells have fairly constant resistances
d, 4	185	528	176	1	cell 1 shows an upward resistance trend, while other cells have fairly constant resistances
e, 5	29	2,166	44	–	flat resistances; cell 1 shows a slightly higher resistance than the other cells when the mean of the selected data is used as a reference point (see Figure S9)
f, 6[a]	1,446[a]	1,352[a]	1,113[a]	8[a]	cell 8 has a slightly higher resistance than the other cells and shows a resistance knee after 3 years[a]
g, 7	15	428	122	5, 7, 8	cells 5, 7, and 8 show different trends in comparison to the other cells
h, 8[a]	1,531[a]	1,923[a]	1,476[a]	–	all cells show a resistance increase close to the end of the available data; seasonal temperature variations are affecting resistance estimates[a]
i, 9[a]	489[a]	534[a]	322[a]	2[a]	after approximately 230 days, cell 2 shows a knee-shaped resistance increase[a]
j, 10[a]	211[a]	417[a]	241[a]	7, 8[a]	cell 8 shows an increasing resistance after 100 days; cell 7 behaves slightly differently from the other cells[a]
k, 11	15	997	185	–	lower average current than most other systems; unclear interpretation
l, 12	93	320	71	8, 7	cells 8 and 7 show different behavior (see also Figure S9); significantly higher temperatures were measured by temperature sensor 4 (see Figure S21)
m, 13	23	724	183	–	lower average current than most other systems; unclear interpretation
n, 14	23	376	117	1	cell 1 shows a lower resistance to the other cells
o, 15	17	1,217	187	–	many data gaps; unclear interpretation
p, 16	34	408	332	4	cell 4 shows a lower resistance to the other cells
q, 17	21	889	218	3	cell 3 shows a much higher resistance to the other cells
r, 18[a]	453[a]	301[a]	182[a]	–	all cells show increasing resistance toward the end of use; unclear interpretation[a]
s, 19	28	712	185	–	lower average current than most other systems; unclear interpretation
t, 20	22	724	183	–	lower average current than most other systems; unclear interpretation
u, 21[a]	1,088[a]	779[a]	377[a]	–	all cells show increasing resistance toward the end of use; unclear interpretation; temperature variations affect resistance estimates[a]

[a]These systems have the highest equivalent full cycle count and are analyzed further.

For ten systems (1, 2, 3, 4, 6, 9, 10, 12, 14, 16, 17), a single cell or two cells behave differently than the remaining cells (Figure 5; Table 2). A single cell shows a knee-shaped resistance behavior for four systems (3, 4, 6, 9). Battery system 8 shows an increasing resistance trajectory for all cells at roughly the same time. Systems 6, 8, and 9 have a high equivalent full cycle count (1,446, 1,531, and 489). Their resistance trajectories suggest that these systems were healthy for most of their operation, with degradation accelerating toward the end of use.

These resistance patterns can have a wide variety of root causes. To further understand the cause of individual degradation, a mechanical inspection of the systems would be needed, which cannot be done because the returned battery systems are not physically available to the authors. Furthermore, the model cannot distinguish between battery degradation, external degradation, or faults such as connector loss, corrosion, connector resistance increase, etc. Learning the battery operating-point-dependent equivalent resistance can be challenging with few data, resulting in larger uncertainty bands. In addition, the output scale parameter of the WV kernel was optimized to track battery degradation (cf., experimental procedures section). Therefore, it can be challenging for the GP to quickly capture sudden faults such as connector loss or others (see Note S4 and Figures S5–S7 for more

details), emphasizing that this method is complementary to faster signal-based fault detection methods.

The operating characteristics, i.e., R(I, SOC, T), modeled by the RBF kernel (Figure S1), are consistent with physical expectations and experimental data from Anseán et al.[53] The current-dependent resistance shows a downward trend with increasing discharge current.[59,60] The SOC-dependent resistance is fairly flat. Some unexpected small upward and downward trends can be attributed to the linear pseudo-OCV (Figure S2). The temperature characteristics show increasing resistance at low and very high temperatures, in line with physical expectations. For a more detailed discussion, see Note S1.

Fault probabilities

Based on the observations on the entire dataset, we investigate how the six systems with the highest equivalent full cycle count (systems 6, 8, 9, 10, 18, and 21) degraded.

Often, only a single cell deviates from the remaining cells (see Table 2; Figure 5). Therefore, we propose defining a battery pack consisting of cells in series to have an acceptable resistance distribution if the internal resistances of each cell are within a resistance band centered around a robust estimate of the mean of the other cells. We use the Hodge-Lehman estimator[61] to estimate the location (i.e., the mean) of cell resistances. The Hodge-Lehman estimator is defined as the median of the mean of all possible pairs of cell resistances, including self-pairs,

$$S_i = \{1, 2, \ldots, n\} \backslash \{i\} \quad \text{(Equation 3)}$$

$$\widehat{\theta}_{R_i}(t) = \text{med}_{j \le k} \frac{R_j(t) + R_k(t)}{2}, j, k \in S_i, \quad \text{(Equation 4)}$$

where $n = 8$, the number of cells. The probability of a cell i to be outside a resistance band that is $2b$ wide is

$$p(F_{R_i}(t)) = p(R_i(t) > \widehat{\theta}_{R_i}(t) + b) + p(R_i(t) < \widehat{\theta}_{R_i}(t) - b). \quad \text{(Equation 5)}$$

The GP provides the mean and probabilities needed to calculate $p(F_{R_i}(t))$. We propose defining the probability of a pack resistance fault, $p(F_{R_p})$, as

$$p\left(F_{R_p}(t)\right) = 1 - \prod_i (1 - p(F_{R_i}(t)(i))) \quad \text{(Equation 6)}$$

according to the true "weakest link" failure statistics for cells connected in series.[62–64] In the limit of failures dominated by a single cell, the pack resistance fault can be approximated by

$$p\left(F_{R_p}(t)\right) \approx \max_i p(F_{R_i}(t)). \quad \text{(Equation 7)}$$

Similarly, battery packs can be faulty or at the end of their life if cells exceed an upper resistance threshold,

$$p(F_{\text{Rm}_i}(t)) = p(R_i(t) > c) \quad \text{(Equation 8)}$$

$$p(F_{\text{Rm}}(t)) = 1 - \prod_i (1 - p(F_{\text{Rm}_i}(t))). \quad \text{(Equation 9)}$$

However, in the following analysis, we only focus on the resistance distribution because the resistance at $t = 0$ differs significantly between systems (Figure 5). The different use cases, with different operating conditions of the systems, can affect the operational

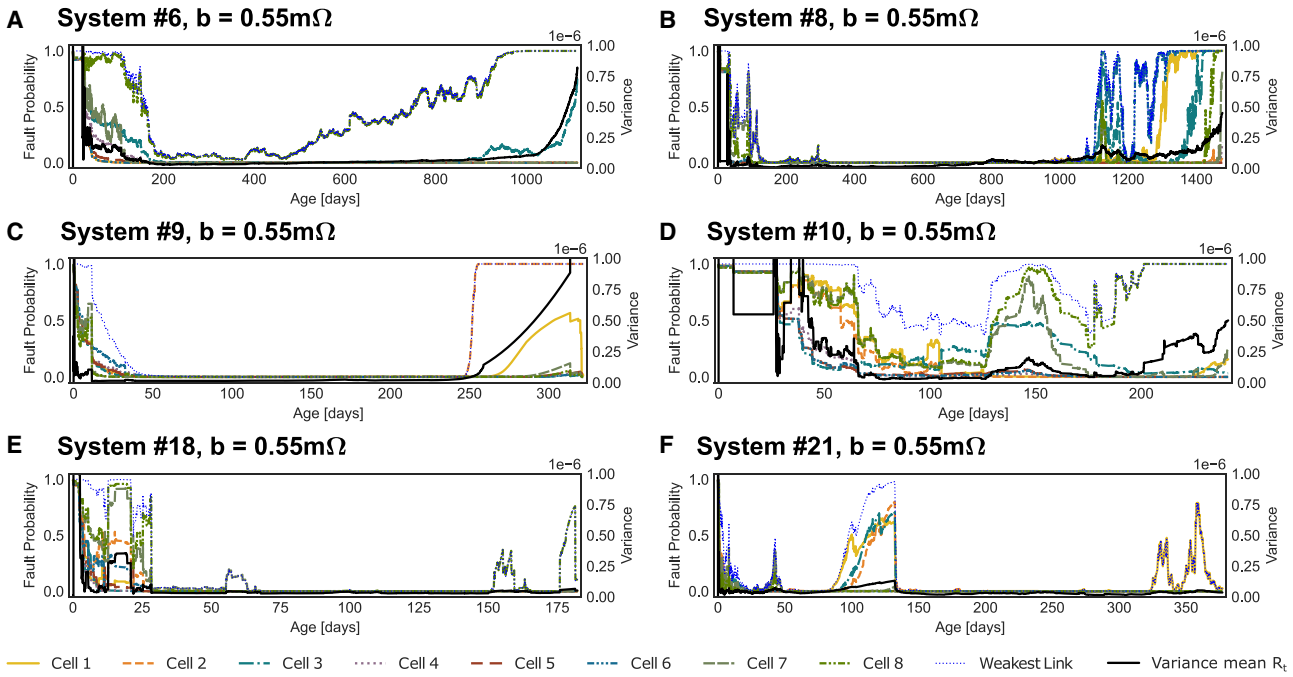

Figure 6. Online forward fault probabilities

Resistance distribution-based fault probabilities for each cell in different colors. Variance of the GP resistance mean in black. Systems 6, 8, 9, 10, 18, and 21 are shown. These systems have the highest equivalent full cycle count. The GP fault probabilities after applying the Rauch-Tung-Striebel smoother are shown in Figure S8.

characteristics learned by the RBF kernel (Figure S1) and lead to such variations. How to address this issue remains an open question for further research.

In an online setting, the ECM-GP needs to be updated continuously as new data arrive. The computational complexity of exact GPs scale with $O(n^3)$, where n is the number of data points, making it computationally infeasible to update the model continuously using all selected data. Therefore, we use a recursive spatiotemporal GP, which scales linearly with the number of data points,[28,46,47] allowing the processing of millions of data points on a laptop computer suitable for use in embedded BMS systems or efficient calculations in the cloud for thousands of systems. Our approach is motivated by the approach developed by Aitio et al.[28] but is not identical. A detailed description of the approach, as well as details on computation time, are given in the experimental procedures section. The spatiotemporal GP walks forward in time using a Kalman filter.

We use the estimate of the Kalman filter at time t_k, which only depends on data up to time t_k to calculate the fault probabilities (Figure 6; see Figure S6 for the corresponding spatiotemporal GP resistance estimates). We set $b = 0.55$ mΩ based on the resistance spread observed at the beginning of the life of the batteries for the investigated systems. The forward fault probabilities (Figure 6) fluctuate more than the GP fault probabilities (Figure S8), which is expected because they only depend on past data. In particular, the forward fault probabilities need a certain amount of data to settle in, here in the order of 30–200 days, depending on the usage of the system. During this initial period, the GP learns the operating point characteristics of the systems (Figure S1). Pre-initializing the matrices of the spatiotemporal GP based on laboratory test data could mitigate this issue. However, here we do not have access to the physical systems, and the systems were operated in very different ways; therefore, pre-initialization is an open question for future work.

System 6: the fault probability of cell 8 is significantly higher than that of the other cells even after the Kalman filter settled in after approximately 200 days. After 500 days, the fault probability of cell 8 starts increasing and crosses 0.5 shortly before 800 days. The remaining cells have a very low fault probability. After 900 days, the fault probabilities of cell 3, the cell with the lowest estimated resistance, increases, too.

System 8: the mean resistances associated with system 8 show seasonal variations (Figure 5H) with higher resistance estimates at lower temperatures despite having a fixed temperature to the operating point. Around 1,100–1,200 days, multiple cell resistance fault probabilities and the weakest link statistic increase sharply, coinciding with the lower temperatures. Around 1,300 days, the weakest link statistic reaches values close to 1, agreeing with the increasing spread between cell resistances. To summarize, system 8 reached an equivalent full cycle count of 1,531 cycles, with seasonal temperature variations but a long-term upward resistance trend with increasingly inhomogeneous resistance as commonly observed by cell-to-cell variability.[50]

System 9: the fault probabilities increase quickly around day 250 for cell 2. In contrast, the other cells have a low fault probability, except for cell 1, which might be affected because it shares a temperature sensor with cell 2.

System 10: the fault probabilities do not settle in. In particular, the resistance probability of cell 8 increases again after 120 days. The fault probabilities suggest that there was an issue early on, in line with the end of use after 211 equivalent full cycles (Table 2).

System 18: the fault probabilities settle in after around 30 days, with only minor fluctuations afterward and some peaks for cell 8 toward the end of use. No clear conclusion is reached by this analysis. .

System 21: the fault probabilities settle in after 50 days. The fault probabilities of cells 1, 2, and 3 increase temporarily around 100–140 days. The fault probabilities of cell 1 increase again after 330. Given the mostly flat and only slightly increasing resistance trend toward the end of use for this system (Figures 5 and S6), no clear conclusion can be reached from it.

The proposed fault probabilities are suitable for analyzing field data and online monitoring. However, a couple of challenges remain, in particular how to mitigate the influence of seasonal temperature variations on the WV kernel and reduce the time it takes for the Kalman filter to settle in. Further investigations are needed to determine how suitable the proposed approach is for the early detection of specific fault types. For example, thermal runaway, the most safety-critical fault, can have different causes. If the cause is abrupt physical damage to the battery, a GP-based approach might struggle to capture it quickly. For such a case, purely signal-based approaches are more suitable because speed is the most important factor. However, if the cause of thermal runaway is slow degradation with partial electrode dry-out and dendrite growth, then there is a chance that such a thermal runaway trigger can be picked up in the resistance change and resistance distribution. The proposed fault probabilities can be used for fault detection; this would require the following: first, a reference operating point; second, a fault probability threshold; third, a band b; and fourth, an upper threshold c. These values should be chosen based on the application and system characteristics, such as cell balancing design, pack

Table 3. Data selection criteria

Charging/discharging	Discharge only
Temperature (°C)	$10 < x < 100$
Current (A)	$-80 < x < -5$
SOC (%)	$40 < x < 95$

layout, and cell-to-cell variability. We did not carry out fault detection because the specific fault types and times are unknown for this dataset.

To summarize, health monitoring, fault analysis, and detection methods are important for the safe operation of battery systems. We use a recursive and exact GP electrical circuit modeling pipeline to analyze faults from field data with measurement noise without precise knowledge of the OCV. The estimated time-dependent equivalent circuit internal resistance is one possible SOH metric for LIB packs. Furthermore, we developed resistance fault probabilities using the individual cell resistance of the cells in a pack, which is suitable for early online monitoring and could be extended into a fault detection framework. The methods are motivated and tested on a large field dataset comprising 28 battery systems and 133 million data rows. The results show that often, a single cell with abnormal performance can cause the end of a system's use and suggest that such faults can be detected with the proposed GP electrical circuit modeling approach. Such an occurrence can be caused after heavy use due to degradation or other issues. Furthermore, the results support that if a cell has a higher resistance early on, then this can already be an indicator that this cell will age faster than the remaining cells. Physically, this could occur by enhanced resistive heating of the most degraded cell, thereby accelerating its degradation,[65] which has been observed in the case of LIBs connected in series.[66] Last, the results suggest that, for larger battery packs, advanced pack layouts that allow the permanent bypass of a more strongly degraded cell can be advantageous in prolonging the life of a system. We outlined several remaining research challenges. To conclude, this analysis furthers the understanding of how batteries degrade and fail in the field and demonstrates the potential of online monitoring. We publish the dataset associated with this article and the software, BattGP, making data and tools for analyzing and modeling battery field data available to the community.

EXPERIMENTAL PROCEDURES

Data selection

The data selection criteria (Table 3) are applied to each cell individually.

GPs

GPs are a flexible modeling framework excelling in the case of limited data by making a point estimate and modeling the covariance associated with the prediction. GPs are nonparametric probabilistic models fully defined by a mean function $\mu(x)$ and a covariance function $k(x,x')$, where $x, x' \in \mathcal{X}^D$. A GP is usually written as

$$f(x) \sim \mathrm{GP}(\mu(x), k(x,x')), \qquad \text{(Equation 10)}$$

making it explicit that GPs describe a distribution of functions. The GP posterior predictions are normally distributed, i.e., any marginal distribution of the GP is Gaussian. Furthermore, all joint distributions associated with a finite number of elements of the index set are multivariate normal distributions. See Williams and Rasmussen[52] for further information. Assuming that we have n_o noisy observations $(x_{o,i}, y_{o,i})$ with $y_{o,i} = f(x_{o,i}) + \epsilon_i$, where ϵ_i is Gaussian noise with variance σ_n^2, the predictive GP equations are

$$\mu_{|o}(X_*) = K(X_*, X_o)\left[K(X_o, X_o)+\sigma_n^2 I\right]^{-1} y_o \quad \text{(Equation 11)}$$

$$\Sigma_{|o}(X_*) = K(X_*, X_*) - K(X_*, X_o)\left[K(X_o, X_o)+\sigma_n^2 I\right]^{-1} K(X_o, X_*), \quad \text{(Equation 12)}$$

where $X_* = [x_{*,1}\cdots x_{*,n_*}]$ denotes the n_* test locations, $X_o = [x_{o,1}\cdots x_{o,n_o}]$ denotes the training locations with responses $y_o^T = [y_{o,1}\cdots y_{o,n_o}]$, and $K(X_1,X_2)$ denotes the covariance matrix that is constructed by applying the kernel function to all pairs of column vectors from X_1 and X_2 (for a full derivation, see Williams and Rasmussen[52]).

The training of a GP refers to the choice of kernel function and the optimization of associated hyperparameters, usually based on optimizing the marginal likelihood of the training data. Subsequently, the posterior distribution can be calculated for points of interest by inference using Equations 11 and 12.

SE kernel

The squared exponential (SE) kernel is a smooth, infinitely many times differentiable kernel that only depends on the distance of data points and is given for 1D x by

$$k_{SE}(x, x') = \sigma_{SE}^2 \exp\left(\frac{-|x - x'|^2}{2l^2}\right). \quad \text{(Equation 13)}$$

We use three input dimensions—current, SOC, and temperature—and combine three 1D RBF kernels to

$$k_{SE,3ARD}(x, x') = \prod_{d=1}^{3} \sigma_{SE,d}^2 \exp\left(\frac{-|x_d - x'_d|^2}{2l_d^2}\right) = \sigma_{SE,3}^2 \exp\left(\sum_{d=1}^{3} \frac{-|x_d - x'_d|^2}{2l_d^2}\right), \quad \text{(Equation 14)}$$

which is known as the SE-ARD kernel (ARD denotes "automatic relevance detection" because each length scale represents the importance of its associated direction; for more information, see Duvenaud[54]). There are four hyperparameters associated with the 3D SE-ARD kernel: the output scale $\sigma_{SE,3}^2$, the length scale associated with the current dimension $l_1 = l_I$, the length scale associated with the SOC dimension $l_2 = l_{SOC}$, and the length scale associated with the temperature dimension $l_3 = l_T$.

WV kernel

The WV model corresponds to the integrated Wiener process.[67] The WV covariance function or kernel is defined by

$$k_{WV}(t, t') = \sigma_{WV}^2\left(\frac{\min^3\{t, t'\}}{3} + |t - t'|\frac{\min^2\{t, t'\}}{2}\right). \quad \text{(Equation 15)}$$

The WV kernel has one hyperparameter: the WV output scale, σ_{WV}^2.

The resulting kernel is

$$k(x, t, x', t') = k_{SE,3ARD}(x, x') + k_{WV}(t, t'). \quad \text{(Equation 16)}$$

Including the noise variance σ_n^2, there are six hyperparameters that define the characteristics of the GP used in this article.

Spatiotemporal GPs

A large number of data points are recorded during the operation of a battery. Ideally, all samples that fulfill the data selection criteria are used, but a classical exact GP prevents this due to the unfavorable scaling of compute and memory usage. To

address this issue, we follow Huber[47] and Solin[67] and leverage the fact that we can interpret the GP as a spatiotemporal GP. For lead-acid batteries, a spatiotemporal GP approach has been shown by Aitio et al.[28]

A temporal GP, i.e., a GP that depends on only one variable, can be written as a Kalman filter,[46,67] which makes it scale linearly with the number of data points, with the restriction that the data points must be given in a sorted manner. Here, the variable is actually time; therefore, this does not impose further restrictions.

A spatiotemporal GP[67] is a GP that depends on multiple variables, one of which can be regarded as the time variable and the others being the spatial variables,

$$x = \begin{bmatrix} t \\ x_s \end{bmatrix}.$$

This concept leads to an infinite-dimensional Kalman filter that propagates the mean and variance functions over the time points. When using only a finite number of spatial vectors, this eventually leads to a classical, finite-dimensional Kalman filter.[67]

We cannot restrict the actual measured data locations to a finite set. Therefore, we combine the spatiotemporal approach with the recursive approach from Huber.[47] In this approach, the spatial part of the GP is not represented exactly but is represented by n_b predefined basis vectors $x_{s,b,i}$ that are collected into

$$X_b = \begin{bmatrix} x_{s,b,1} & x_{s,b,2} & \cdots & x_{s,b,n_b} \end{bmatrix}.$$

Combining these two approaches leads to the following procedure, which is similar but not identical to the method used by Aitio et al.[28] The difference is mentioned below.

The state z of the Kalman filter,

$$z = \begin{bmatrix} z_t \\ z_s \end{bmatrix},$$

comprises two parts. z_t corresponds to the representation of the temporal kernel. In the case of the WV kernel, it contains two scalar values: the first represents the mean value, and the second is the time derivative of the mean value.[67] z_s corresponds to the spatial kernel, and for the Huber approach,[47] these are the mean values at the specified basis vectors X_b.

Evaluation

Given the state $z_{k|k}$ and its covariance matrix $P_{k|k}$ at the time t_k and built with all information available until t_k, the mean and covariance at this time point can be calculated by

$$\mu_{|k}(X_q, t_k) = Hz_{k|k} \qquad \text{(Equation 17)}$$

$$\Sigma_{|k}(X_q, t_k) = K_{qq} + HP_{k|k}H^T - H_s K_{bb} H_s^T. \qquad \text{(Equation 18)}$$

The mean and the covariance of the GP at n_q spatial vectors $x_{s,q,i}$ are collected into X_q similar to X_b. Furthermore, we use the abbreviations

$$K_{bb} \in \mathbb{R}^{n_b \times n_b}, (K_{bb})_{i,j} = k_s(x_{s,b,i}, x_{s,b,j}) \text{ and}$$
$$K_{qq} \in \mathbb{R}^{n_q \times n_q}, (K_{qq})_{i,j} = k_s(x_{s,q,i}, x_{s,q,j})$$

for the covariance at the basis vectors and the covariance at the queried locations, respectively.

The measurement matrix

$$H = [H_t \quad H_s] \tag{Equation 19}$$

is partitioned according to z. The temporal part

$$H_t = \begin{bmatrix} 1 & 0 \\ \vdots & \vdots \\ 1 & 0 \end{bmatrix} \tag{Equation 20}$$

reflects that for the WV kernel with the chosen representation, the first associated state corresponds to the mean. The spatial part is

$$H_s = K_{qb} K_{bb}^{-1}, \tag{Equation 21}$$

with

$$K_{qb} \in \mathbb{R}^{n_q \times n_b}, \left(K_{qb}\right)_{i,j} = k_s\left(x_{s,q,i}, x_{s,b,j}\right)$$

given by Huber.[47] Here, our approach differs from the approach described by Aitio et al.[28] In Equation 21, only the inverse of K_{bb} is needed, which is known *a priori* and can be calculated offline. The corresponding term used by Aitio et al.[28] includes an additional part that depends on the current state; thus, the inverse must be calculated in each step anew.

Prediction step

The prediction step of the Kalman filter is performed identically to Aitio et al.,[28]

$$z_{k|k-1} = A(T_s) z_{k-1|k-1}$$

$$P_{k|k-1} = A(T_s) P_{k-1|k-1} A^T(T_s) + Q(T_s),$$

with

$$P(0) = \begin{bmatrix} P_t(0) & 0 \\ 0 & P_s(0) \end{bmatrix}, A(T_s) = \begin{bmatrix} A_t(T_s) & 0 \\ 0 & I \end{bmatrix}, \text{and } Q(T_s) = \begin{bmatrix} Q_t(T_s) & 0 \\ 0 & 0 \end{bmatrix},$$

where $T_s = t_k - t_{k-1}$ is the length of the time step that may be different for each prediction step. The structure of these matrices shows the decoupling of the two parts, i.e., the spatial state is not influenced by the time step. However, due to the correction step, the covariance matrix will not retain its initial block diagonal structure.

For the WV kernel (Equation 15), which is used as temporal kernel, the corresponding matrices are

$$P_t(0) = \begin{bmatrix} 0 & 0 \\ 0 & 0 \end{bmatrix}, A_t(T_s) = \begin{bmatrix} 1 & T_s \\ 0 & 1 \end{bmatrix} \text{ and } Q_t(T_s) = \sigma_{WV}^2 = \begin{bmatrix} T_s^3/3 & T_s^2/2 \\ T_s^2/2 & T_s \end{bmatrix}.$$

The initial value for the spatial covariance matrix is $P_s(0) = K_{bb}$.[28,67]

Correction step

When new measurements $(X_{m,k}, y_{m,k})$ arrive, the Kalman filter performs a correction step

$$z_{k|k} = z_{k|k-1} + K_k\left(y_{m,k} - H_k z_{k|k-1}\right)$$
$$P_{k|k} = P_{k|k-1} - K_k H_k P_{k|k-1}.$$

$X_{m,k}$ is a matrix that contains the locations of the $n_{m,k}$ measurements, $y_{m,k}$ is a vector giving the measured output for each location in $X_{m,k}$, and H_k is the measurement matrix build as in Equation 19 with $X_q = X_{m,k}$. The Kalman gain K_k is calculated by

$$K_k = P_{k|k-1} H_k^T \left(\Sigma_{|k}(X_{m,k}) + \sigma_n^2 I\right)^{-1}, \quad \text{(Equation 22)}$$

where $\Sigma_{|k}(X_{m,k})$ is given by Equation 18 with $X_q = X_{m,k}$. This step differs from Aitio et al.[28] by the different evaluation mentioned above and another measurement model.

Remark 1

If $n_{m,k} = 0$, i.e., no measurement data were acquired within the last time step, the correction step can be skipped, and the algorithm proceeds with the next prediction step. Alternatively, the algorithm could wait until new data are available and then perform a larger prediction step.

Remark 2

In a standard Kalman filter setup, the correction step can be performed iteratively for each group of measurements that is not correlated with measurements outside this group. Consequently, for the case here, where we model the measurement noise with the covariance matrix $\sigma_n^2 I$, i.e., all measurements are uncorrelated, each measurement could be processed individually, thus rendering the matrix inverse in Equation 22 a scalar inversion. However, due to some simplifications in the approach of Huber[47] that led to the filter equations, processing each measurement individually or multiple measurements together in a minibatch is not analytically equivalent for this application. Based on case studies, it seems to be advantageous to add measurements in larger groups.

RTS smoother

The Rauch-Tung-Striebel (RTS) smoother allows for the calculation of the state and covariance and, thus, the estimates $\mu_{|n}(X_q, t_k)$ and $\Sigma_{|n}(X_q, t_k)$ at all time points t_k under consideration of the complete measured data of the n time points. This smoother starts with the variables $z_{n|n}$ and $P_{n|n}$ of the last Kalman filter correction step and iterates backward[68] using

$$z_{k|n} = z_{k|k} + G_k \left(z_{k+1|n} - z_{k+1|k}\right) \quad \text{(Equation 23)}$$

$$P_{k|n} = P_{k|k} + G_k \left(P_{k+1|n} - P_{k+1|k}\right) G_k^T \quad \text{(Equation 24)}$$

for $k = n - 1, n - 2, \ldots$ with

$$G_k = P_{k|k} A (t_{k+1} - t_k) P_{k+1|k}^{-1}. \quad \text{(Equation 25)}$$

The output values $\mu_{|n}(X_q, t_k)$ and their variances $\Sigma_{|n}(X_q, t_k)$ for each time point t_k can be calculated by Equations 17 and 18 by replacing $z_{k|k}$ with $z_{k|n}$ and $P_{k|k}$ with $P_{k|n}$.

To evaluate Equations 23, 24, and 25, the values $z_{k|k}$ and $P_{k|k}$ calculated by the forward pass of the Kalman filter are needed. Thus, these values must be stored while performing the forward filtering pass. $z_{k+1|k}$ and $P_{k+1|k}$ could be either stored also or calculated anew from $z_{k|k}$ and $P_{k|k}$ by reevaluating the prediction step.

Implementation

The batteries are mostly sampled with 5 s, which, with the very small magnitude of sensible parameters for the output scale of the WV kernel, leads to numerical issues in performing the prediction steps.

Therefore, we define a sampling time for the updates (1 h) and process all data captured within this interval at the same update time point. If no data were recorded within this hour, then we only performed a new prediction step without the update to set an evaluation point for the later backward smoothing pass.

Selection of basis vectors

The selection of basis vectors can be done in different ways. Similar to Aitio et al.,[28] we found that using k-means to select the basis vectors is effective, i.e., the results and confidence intervals of the spatiotemporal GP with 36 basis vectors selected by k-means as well as the reference operating point, resulting in 37 basis vectors, resemble fairly closely the results of the full GP with up to 40,000 data points (compare Figures S4 and 5). To calculate the fault probabilities, we use 60 basis vectors selected with k-means. However, in an online setting, there will be no data available at the beginning. Therefore, as an alternative, we propose placing vectors linearly within the range of the data selection criteria and setting a constraint based on the length scale of the associated measurement (see Note S3 for more details).

Hyperparameter tuning

All battery systems contain the same prismatic cell type with the same specifications. Therefore, the aim is to find a single hyperparameter set that can be used for all cells. We optimized the marginal likelihood for all cells of systems 6 and 8 individually using an exact GP and 20,000 data points for each cell. Systems 6 and 8 have the highest equivalent full cycle counts and were operated over a large temperature range. Subsequently, we chose the median of each hyperparameter, assuming that the parameters are mutually independent. We do not formulate an optimization problem for the spatiotemporal GP but use the hyperparameters found by the exact GP.

Software and hardware details

The full GP is solved on an NVIDIA A100 GPU with 80 GB RAM. We use the Python GPytorch framework, allowing us to solve an exact GP with 40,000 data points in 11 s on average. The recursive GP is solved on a MacBook Pro with a 10-core M1 chip, taking approximately 22 s for the forward Kalman filter and 6 s for the RTS smoother for a single cell of system 8 with 35,000 time steps, 320,000 data points, and 61 basis points.

RESOURCE AVAILABILITY

Lead contact

Requests for further information and resources should be directed to and will be fulfilled by the lead contact, Rolf Findeisen (rolf.findeisen@iat.tu-darmstadt.de).

Materials availability

This study did not generate new unique reagents.

Data and code availability

- The latest version of the associated Python software BattGP is available on GitHub (https://github.com/JoachimSchaeffer/BattGP).
- The dataset is available on Zenodo (https://zenodo.org/records/13715694).

ACKNOWLEDGMENTS

We would like to thank numerous people from the data provider for their outstanding support throughout this project; however, we cannot name them due to the condition of anonymity from the data provider. In particular, we are truly grateful for the outstanding support from our initial

contact person at the data provider; without you, this work would not have been possible. The work was financed through base funding from the Technical University of Darmstadt.

AUTHOR CONTRIBUTIONS

Conceptualization, J.S.; methodology, J.S., E.L., and D.G.; software, J.S., E.L., and D.G.; validation, J.S.; formal analysis, J.S. and E.L.; investigation, J.S. and D.G.; data curation, J.S. and D.G.; writing – original draft, J.S.; writing – review & editing, J.S., E.L., D.G., M.Z.B., R.D.B., and R.F.; visualization, J.S. and E.L.; supervision, R.D.B. and R.F.; resources, R.F.; funding acquisition, R.F.

DECLARATION OF INTERESTS

The authors declare no competing interests.

SUPPLEMENTAL INFORMATION

Supplemental information can be found online at https://doi.org/10.1016/j.xcrp.2024.102258.

Received: May 28, 2024
Revised: August 21, 2024
Accepted: September 28, 2024
Published: October 25, 2024

REFERENCES

1. Blomgren, G.E. (2016). The development and future of lithium ion batteries. J. Electrochem. Soc. *164*, A5019–A5025. https://doi.org/10.1149/2.0251701jes.

2. European Union (2023). Regulation (eu) 2023/1542 of the european parliament and of the council of 12 july 2023 concerning concerning batteries and waste batteries, amending directive 2008/98/ec and regulation (eu) 2019/1020 and repealing directive 2006/66/ec. O.J. L 191/1 66, 1–117. https://eur-lex.europa.eu/eli/reg/2023/1542/oj.

3. Hanicke, M., Ibrahim, D., Jautelat, S., Torscht, L., van de Rijt, A., Linder, M., and Schaufuss, P. (2023). Battery demand is growing–and so is the need for better solutions along the value chain. https://www.mckinsey.com/industries/automotive-and-assembly/our-insights/battery-2030-resilient-sustainable-and-circular.

4. Sun, P., Bisschop, R., Niu, H., and Huang, X. (2020). A review of battery fires in electric vehicles. Fire Technol. *56*, 1361–1410. https://doi.org/10.1007/s10694-020-00958-2.

5. Im, D.-H., and Chung, J.-B. (2023). Social construction of fire accidents in battery energy storage systems in korea. J. Energy Storage *71*, 108192. https://doi.org/10.1016/j.est.2023.108192.

6. Hu, W. (2023). How New York plans to regulate e-bikes in the wake of deadly fires. The New York Times. September 15, 2023. https://www.nytimes.com/article/ebike-laws-nyc.html.

7. Sulzer, V., Mohtat, P., Aitio, A., Lee, S., Yeh, Y.T., Steinbacher, F., Khan, M.U., Lee, J.W., Siegel, J.B., Stefanopoulou, A.G., and Howey, D.A. (2021). The challenge and opportunity of battery lifetime prediction from field data. Joule *5*, 1934–1955. https://doi.org/10.1016/j.joule.2021.06.005.

8. Plett, G.L. (2015). Battery Management Systems: Equivalent-Circuit Methods, *2* (Artech House).

9. Li, W., Rentemeister, M., Badeda, J., Jöst, D., Schulte, D., and Sauer, D.U. (2020). Digital twin for battery systems: Cloud battery management system with online state-of-charge and state-of-health estimation. J. Energy Storage *30*, 101557. https://doi.org/10.1016/j.est.2020.101557.

10. Pozzato, G., Allam, A., Pulvirenti, L., Negoita, G.A., Paxton, W.A., and Onori, S. (2023). Analysis and key findings from real-world electric vehicle field data. Joule *7*, 2035–2053. https://doi.org/10.1016/j.joule.2023.07.018.

11. Ward, L., Babinec, S., Dufek, E.J., Howey, D.A., Viswanathan, V., Aykol, M., Beck, D.A., Blaiszik, B., Chen, B.-R., Crabtree, G., et al. (2022). Principles of the battery data genome. Joule *6*, 2253–2271. https://doi.org/10.1016/j.joule.2022.08.008.

12. Schaeffer, J., Galuppini, G., Rhyu, J., Asinger, P.A., Droop, R., Findeisen, R., and Braatz, R.D. (2024). Cycle life prediction for lithium-ion batteries: Machine learning and more. arXiv. https://arxiv.org/abs/2404.04049

13. Krewer, U., Röder, F., Harinath, E., Braatz, R.D., Bedürftig, B., and Findeisen, R. (2018). Dynamic models of li-ion batteries for diagnosis and operation: A review and perspective. J. Electrochem. Soc. *165*, A3656–A3673. https://doi.org/10.1149/2.1061814jes.

14. Ramadesigan, V., Northrop, P.W.C., De, S., Santhanagopalan, S., Braatz, R.D., and Subramanian, V.R. (2012). Modeling and simulation of lithium-ion batteries from a systems engineering perspective. J. Electrochem. Soc. *159*, R31–R45. https://doi.org/10.1149/2.018203jes.

15. Petit, M., Prada, E., and Sauvant-Moynot, V. (2016). Development of an empirical aging model for li-ion batteries and application to assess the impact of vehicle-to-grid strategies on battery lifetime. Appl. Energy *172*, 398–407. https://doi.org/10.1016/j.apenergy.2016.03.119.

16. Samadani, E., Farhad, S., Scott, W., Mastali, M., Gimenez, L.E., Fowler, M., and Fraser, R.A. (2015). Empirical modeling of lithium-ion batteries based on electrochemical impedance spectroscopy tests. Electrochim. Acta *160*, 169–177. https://doi.org/10.1016/j.electacta.2015.02.021.

17. Severson, K.A., Attia, P.M., Jin, N., Perkins, N., Jiang, B., Yang, Z., Chen, M.H., Aykol, M., Herring, P.K., Fraggedakis, D., et al. (2019). Data-driven prediction of battery cycle life before capacity degradation. Nat. Energy *4*, 383–391. https://doi.org/10.1038/s41560-019-0356-8.

18. Jones, P.K., Stimming, U., and Lee, A.A. (2022). Impedance-based forecasting of lithium-ion battery performance amid uneven usage. Nat. Commun. *13*, 4806. https://doi.org/10.1038/s41467-022-32422-w.

19. Schaeffer, J., Gasper, P., Garcia-Tamayo, E., Gasper, R., Adachi, M., Pablo Gaviria-Cardona, J., Montoya-Bedoya, S., Bhutani, A., Schiek, A., Goodall, R., et al. (2023). Machine learning benchmarks for the classification of equivalent circuit models from solid-state electrochemical impedance spectra. J. Electrochem. Soc. *170*, 060512. https://doi.org/10.1149/1945-7111/acd8fb.

20. Schaeffer, J., Lenz, E., Chueh, W.C., Bazant, M.Z., Findeisen, R., and Braatz, R.D. (2024). Interpretation of high-dimensional linear regression: Effects of nullspace and regularization demonstrated on battery data. Comput. Chem. Eng. *180*, 108471. https://doi.org/10.1016/j.compchemeng.2023.108471.

21. Richardson, R.R., Osborne, M.A., and Howey, D.A. (2017). Gaussian process regression for forecasting battery state of health. J. Power Sources *357*, 209–219. https://doi.org/10.1016/j.jpowsour.2017.05.004.

22. Richardson, R.R., Birkl, C.R., Osborne, M.A., and Howey, D.A. (2019). Gaussian process regression for in situ capacity estimation of

lithium-ion batteries. IEEE Trans. Ind. Inf. *15*, 127–138. https://doi.org/10.1109/TII.2018.2794997.

23. Newman, J., and Tiedemann, W. (1975). Porous-electrode theory with battery applications. AIChE J. *21*, 25–41. https://doi.org/10.1002/aic.690210103.

24. Doyle, M., Fuller, T.F., and Newman, J. (1993). Modeling of galvanostatic charge and discharge of the lithium/polymer/insertion cell. J. Electrochem. Soc. *140*, 1526–1533. https://doi.org/10.1149/1.2221597.

25. Jokar, A., Rajabloo, B., Désilets, M., and Lacroix, M. (2016). Review of simplified Pseudo-two-Dimensional models of lithium-ion batteries. J. Power Sources *327*, 44–55. https://doi.org/10.1016/j.jpowsour.2016.07.036.

26. Aykol, M., Gopal, C.B., Anapolsky, A., Herring, P.K., van Vlijmen, B., Berliner, M.D., Bazant, M.Z., Braatz, R.D., Chueh, W.C., and Storey, B.D. (2021). Perspective—Combining physics and machine learning to predict battery lifetime. J. Electrochem. Soc. *168*, 030525. https://doi.org/10.1149/1945-7111/abec55.

27. Nascimento, R.G., Corbetta, M., Kulkarni, C.S., and Viana, F.A. (2021). Hybrid physics-informed neural networks for lithium-ion battery modeling and prognosis. J. Power Sources *513*, 230526. https://doi.org/10.1016/j.jpowsour.2021.230526.

28. Aitio, A., and Howey, D.A. (2021). Predicting battery end of life from solar off-grid system field data using machine learning. Joule *5*, 3204–3220. https://doi.org/10.1016/j.joule.2021.11.006.

29. Hu, X., Zhang, K., Liu, K., Lin, X., Dey, S., and Onori, S. (2020). Advanced fault diagnosis for lithium-ion battery systems: A review of fault mechanisms, fault features, and diagnosis procedures. EEE. Ind. Electron. Mag. *14*, 65–91. https://doi.org/10.1109/MIE.2020.2964814.

30. Wang, Q., Mao, B., Stoliarov, S.I., and Sun, J. (2019). A review of lithium ion battery failure mechanisms and fire prevention strategies. Prog. Energy Combust. Sci. *73*, 95–131. https://doi.org/10.1016/j.pecs.2019.03.002.

31. Tran, M.-K., and Fowler, M. (2020). A review of lithium-ion battery fault diagnostic algorithms: Current progress and future challenges. Algorithms *13*, 62. https://doi.org/10.3390/a13030062.

32. Jiang, L., Deng, Z., Tang, X., Hu, L., Lin, X., and Hu, X. (2021). Data-driven fault diagnosis and thermal runaway warning for battery packs using real-world vehicle data. Energy *234*, 121266. https://doi.org/10.1016/j.energy.2021.121266.

33. Kang, Y., Duan, B., Zhou, Z., Shang, Y., and Zhang, C. (2020). Online multi-fault detection and diagnosis for battery packs in electric vehicles. Appl. Energy *259*, 114170. https://doi.org/10.1016/j.apenergy.2019.114170.

34. Li, X., and Wang, Z. (2018). A novel fault diagnosis method for lithium-ion battery packs of electric vehicles. Measurement *116*, 402–411. https://doi.org/10.1016/j.measurement.2017.11.034.

35. Li, X., Dai, K., Wang, Z., and Han, W. (2020). Lithium-ion batteries fault diagnostic for electric vehicles using sample entropy analysis method. J. Energy Storage *27*, 101121. https://doi.org/10.1016/j.est.2019.101121.

36. Chen, Z., Xiong, R., Tian, J., Shang, X., and Lu, J. (2016). Model-based fault diagnosis approach on external short circuit of lithium-ion battery used in electric vehicles. Appl. Energy *184*, 365—–374. https://doi.org/10.1016/j.apenergy.2016.10.026.

37. Zhang, K., Hu, X., Liu, Y., Lin, X., and Liu, W. (2022). Multi-fault detection and isolation for lithium-ion battery systems. IEEE Trans. Power Electron. *37*, 971–989. https://doi.org/10.1109/TPEL.2021.3098445.

38. Sadhukhan, C., Mitra, S.K., Bhattacharyya, S., Almatrafi, E., Saleh, B., and Naskar, M.K. (2022). Modeling and simulation of high energy density lithium-ion battery for multiple fault detection. Sci. Rep. *12*, 9800. https://doi.org/10.1038/s41598-022-13771-4.

39. Zhao, Y., Liu, P., Wang, Z., Zhang, L., and Hong, J. (2017). Fault and defect diagnosis of battery for electric vehicles based on big data analysis methods. Appl. Energy *207*, 354–362. https://doi.org/10.1016/j.apenergy.2017.05.139.

40. Samanta, A., Chowdhuri, S., and Williamson, S.S. (2021). Machine learning-based data-driven fault detection/diagnosis of lithium-ion battery: A critical review. Electronics *10*, 1309. https://doi.org/10.3390/electronics10111309.

41. Schmid, M., Kneidinger, H.-G., and Endisch, C. (2021). Data-driven fault diagnosis in battery systems through cross-cell monitoring. IEEE Sens. J. *21*, 1829–1837. https://doi.org/10.1109/JSEN.2020.3017812.

42. Zhao, J., Ling, H., Wang, J., Burke, A.F., and Lian, Y. (2022). Data-driven prediction of battery failure for electric vehicles. iScience *25*, 104172. https://doi.org/10.1016/j.isci.2022.104172.

43. Xiong, R., Li, L., and Tian, J. (2018). Towards a smarter battery management system: A critical review on battery state of health monitoring methods. J. Power Sources *405*, 18–29. https://doi.org/10.1016/j.jpowsour.2018.10.019.

44. Berecibar, M., Gandiaga, I., Villarreal, I., Omar, N., Van Mierlo, J., and Van den Bossche, P. (2016). Critical review of state of health estimation methods of li-ion batteries for real applications. Renew. Sustain. Energy Rev. *56*, 572–587. https://doi.org/10.1016/j.rser.2015.11.042.

45. Attia, P.M., Bills, A., Brosa Planella, F., Dechent, P., dos Reis, G., Dubarry, M., Gasper, P., Gilchrist, R., Greenbank, S., Howey, D., et al. (2022). Review—"knees" in lithium-ion battery aging trajectories. J. Electrochem. Soc. *169*, 060517. https://doi.org/10.1149/1945-7111/ac6d13.

46. Särkkä, S., Solin, A., and Hartikainen, J. (2013). Spatiotemporal learning via infinite-dimensional Bayesian filtering and smoothing: A look at Gaussian process regression through Kalman filtering. IEEE Signal Process. Mag. *30*, 51–61. https://doi.org/10.1109/MSP.2013.2246292.

47. Huber, M.F. (2014). Recursive Gaussian process: On-line regression and learning. Pattern Recogn. Lett. *45*, 85–91. https://doi.org/10.1016/j.patrec.2014.03.004.

48. Aitio, A., Jöst, D., Sauer, D.U., and Howey, D.A. (2023). Learning battery model parameter dynamics from data with recursive gaussian process regression. arXiv. https://doi.org/10.48550/arXiv.2304.13666.arXiv.preprint.

49. Figgener, J., van Ouwerkerk, J., Haberschusz, D., Bors, J., Woerner, P., Mennekes, M., Hildenbrand, F., Hecht, C., Kairies, K.P., Wessels, O., and Sauer, D.U. (2024). Multi-year field measurements of home storage systems and their use in capacity estimation. Nat. Energy, 1–10. https://doi.org/10.1038/s41560-024-01620-9.

50. Beck, D., Dechent, P., Junker, M., Sauer, D.U., and Dubarry, M. (2021). Inhomogeneities and cell-to-cell variations in lithium-ion batteries, a review. Energies *14*, 3276. https://doi.org/10.3390/en14113276.

51. Barbers, E., Hust, F.E., Hildenbrand, F.E.A., Frie, F., Quade, K.L., Bihn, S., Sauer, D.U., and Dechent, P. (2024). Exploring the effects of cell-to-cell variability on battery aging through stochastic simulation techniques. J. Energy Storage *84*, 110851. https://doi.org/10.1016/j.est.2024.110851.

52. Williams, C.K.I., and Rasmussen, C.E. (2006). Gaussian Processes for Machine Learning, *2* (MIT Press).

53. Anseán, D., García, V.M., González, M., Viera, J.C., Blanco, C., and Antuña, J.L. (2013). DC internal resistance during charge: Analysis and study on LiFePO 4batteries. World Electric Vehicle Symposium and Exhibition (EVS27), 1–11. https://doi.org/10.1109/EVS.2013.6914746.

54. Duvenaud, D. (2014). Automatic Model Construction with Gaussian Processes (Ph.D. thesis University of Cambridge UK).

55. Cogswell, D.A., and Bazant, M.Z. (2013). Theory of coherent nucleation in phase-separating nanoparticles. Nano Lett. *13*, 3036–3041. https://doi.org/10.1021/nl400497t.

56. Ferguson, T.R., and Bazant, M.Z. (2014). Phase transformation dynamics in porous battery electrodes. Electrochim. Acta *146*, 89–97. https://doi.org/10.1016/j.electacta.2014.08.083.

57. Islam, S.M.R., Park, S.-Y., and Balasingam, B. (2020). Unification of internal resistance estimation methods for li-ion batteries using hysteresis-free equivalent circuit models. Batteries *6*, 32. https://doi.org/10.3390/batteries6020032.

58. Ludwig, S., Zilberman, I., Horsche, M.F., Wohlers, T., and Jossen, A. (2021). Pulse resistance based online temperature estimation for lithium-ion cells. J. Power Sources *490*, 229523. https://doi.org/10.1016/j.jpowsour.2021.229523.

59. Bai, P., and Bazant, M.Z. (2014). Charge transfer kinetics at the solid–solid interface in porous electrodes. Nat. Commun. *5*, 3585. https://doi.org/10.1038/ncomms4585.

60. Bazant, M.Z. (2023). Unified quantum theory of electrochemical kinetics by

coupled ion–electron transfer. Faraday Discuss *246*, 60–124. https://doi.org/10.1039/D3FD00108C.

61. Jr, J.L.H., and Lehmann, E.L. (1963). Estimates of location based on rank tests. Ann. Math. Stat. *34*, 598–611. https://doi.org/10.1214/aoms/1177704172.

62. Gumbel, E.J. (1958). Statistics of Extremes (Columbia University Press).

63. Fisher, R.A., and Tippett, L.H.C. (1928). Limiting forms of the frequency distribution of the largest or smallest member of a sample. Math. Proc. Camb. Phil. Soc. *24*, 180–190. https://doi.org/10.1017/S0305004100015681.

64. Le, J.-L., Bažant, Z.P., and Bazant, M.Z. (2009). Lifetime of high-k gate dielectrics and analogy with strength of quasibrittle structures. J. Appl. Phys. *106*, 104119. https://doi.org/10.1063/1.3256225.

65. Gogoana, R., Pinson, M.B., Bazant, M.Z., and Sarma, S.E. (2014). Internal resistance matching for parallel-connected lithium-ion cells and impacts on battery pack cycle life. J. Power Sources *252*, 8–13. https://doi.org/10.1016/j.jpowsour.2013.11.101.

66. Chiu, K.-C., Lin, C.-H., Yeh, S.-F., Lin, Y.-H., Huang, C.-S., and Chen, K.-C. (2014). Cycle life analysis of series connected lithium-ion batteries with temperature difference. J. Power Sources *263*, 75–84. https://doi.org/10.1016/j.jpowsour.2014.04.034.

67. Solin, A. (2016). Stochastic Differential Equation Methods for Spatio-Temporal Gaussian Process Regression (Ph.D. thesis Aalto University). https://aaltodoc.aalto.fi/handle/123456789/19842AaltoUniversitypublicationseries DoctoralDissertations, 50/2016.

68. Särkkä, S., and Solin, A. (2019). Applied Stochastic Differential Equations (Cambridge University Press).